INTERNATIONAL JOURNAL OF MARITIME TECHNOLOGY
IJMT Vol.3/ Winter 2015 (41-47)

Available online at: http://ijmt.ir/browse.php?a_code=A-10-179-2&sid=1&slc_lang=en

Investigation of Keel Curvature Effect on the Hydrodynamic Characteristics of a V-Shaped Planing Surface

Hashem Moradi[1], Amir Hossein Nikseresht[2*], Alireza Mostofizadeh[3]

[1] *Faculty of Marine Engineering, Amirkabir University of Technology, Hafez Avenue, Tehran, Iran*
[2*] *Faculty of Mechanical and Aerospace Engineering, Shiraz University of Technology, Modares Blvd. Shiraz, Iran. Nikser@sutech.ac.ir*
[3] *Faculty of Mechanical and Aerospace Engineering, Malek-ashtar University of Technology, Isfahan, Iran.*

ARTICLE INFO

Article History:
Received: 13 Sep. 2014
Accepted: 14 Apr. 2015
Available online: 20 Jun. 2015

Keywords:
Free surface
Turbulent
NACA
VOF
Wedge

ABSTRACT

In this paper, three-dimensional two phase turbulent free surface flow is solved by an in-house code. The incompressible Reynolds average Navier-Stocks equations (RANS) with k-ε turbulence model are solved by the finite volume method in the non-orthogonal curvilinear coordinates. For the modeling of the free surface effect, Lagrangian propagation volume tracking method (VOF-PLIC) is used. The code is validated solving two-phase turbulent flow through the impact problem of a circular cylinder. Then, the horizontal movement of a NACA standard wedge with 20 degree deadrise angle is simulated. The flow field and generated waves is estimated with different velocities. Numerical results of the average wetted lengths show acceptable compatibilities with the available experimental data. In addition, some modifications on the V-bottom are done to investigate the effect of the keel curvature and deadrise angle on the hydrodynamic forces. In each cases the ratio of the lift and drag coefficient to the conventional wedge with 20 degree deadrise angle is evaluated. It is depicted that the convex curvature doubles the drag coefficient and has not any significant effect on the lift coefficient. The results confirm that the deadrise angle reduction decreases the needed engine power in take-off. However, this reduction has a destructive effect at the time of landing.

1. Introduction

Calculating the flow field around a vessel is an important step in hull design and vessel shape optimization. One of the major hydrodynamic points in such problems is the appropriate designing of the keel profile.

In free surface problems the effect of both water and air phases should be taken into account and computing the free surface shape is necessary. Predicting free surface profile is complicated and also some methods of predicting free surface profile do not have the ability of modeling the different types of flow fields effectively. Therefore, choosing a suitable method depends on several options such as geometry, conditions of the flow field, method performance and numerical equipments.

Gao *et al.* [1] used a two-layered model to study the oil and air flow in a pipe. They associated the Low Reynolds model with Jones and Launder [2] model in the wall adjacency and used RNG *k-ε* model in the farther region. Meanwhile, the VOF-PLIC method was applied to obtain free surface profile. Their results were good except near the free surface due to the average amount of properties of the two fluids on a joint surface.

The impact of water wave with the coastline was studied by Yuk *et al*. [3]. They have used anisotropic k-ε model with a wall function and the VOF method for predicting the free surface profile. They have predicted the wave profile before and during the wave fracture with some errors because of the wave random movement in the fracture. Ciortan *et al.* [4] used LES and algebraic turbulence model of Baldwin Lomax to calculate the flow field around the Wigley body and used the surface tracking method to obtain the free surface profile. They have showed that the predicted wave height distributions with the LES method is in better agreement in comparison with Baldwin Lomax, which is an incomplete algebraic model.

Rhee *et al.* [5] have assessed the wave flow around a surface-piercing foil using Fluent software, with the VOF scheme and realizable *k-ε* model. They

[Downloaded from ijmt.ir on 2026-11-23]

illustrated that VOF scheme could be used for a wide range of free surface wave types.

VOF and LES or different *k-ε* models are the most appropriate method for free surface profile and two-phase turbulent flow, respectively. However, Experimental data confirm the need of new research and modification in models to correct constant coefficients and damping functions.

In the present work, an in-house code is developed to solve the Reynolds average Navier-stocks (RANS) equations using the finite volume method in incompressible, laminar and turbulent flows considering the free surface flow in general non-orthogonal curvilinear coordinates. First, in order to validate the code in the two-phase flow, the impact problem of a circular cylinder in the turbulent flow regimes is analyzed. Then, as a practical and applicable model, three-dimensional movement of the standard NACA wedge which has the same geometry as the keel of flying boats is investigated. Furthermore, to optimize the keel curvature, some geometric modifications are applied and corresponding effects on the drag and lift forces are studied.

2. Governing Equations

Flow around a ship hulls is governed by the incompressible form of Navier-Stocks equations. The standard k-ε model was applied for RANS simulations in this study.

The non-dimensional variables are defined as follows [6]:

$$x^* = \frac{x}{L},\ y^* = \frac{y}{L},\ z^* = \frac{z}{L},\ t^* = \left(\frac{U_\infty}{L}\right)t,\ \mu^* = \frac{\mu}{\mu_l},$$
$$\rho^* = \frac{\rho}{\rho_l},\ U^* = \frac{U}{U_\infty},\ p^* = \frac{p - p_\infty}{\rho_l U_\infty^2},\ \mathrm{Re} = \frac{\rho_l U_\infty L}{\mu_l},\quad (1)$$
$$Fr = \frac{U_\infty}{\sqrt{gL}},\ \mu_T^* = \frac{\mu_T}{\mu_l},\ k^* = \frac{k}{U_\infty^2},\ \varepsilon^* = \frac{\varepsilon\,\mathrm{L}}{U_\infty^3}$$

and then, the dimensionless equations is used (for simplicity * is omitted):

$$\frac{\partial \rho \bar{u}_i}{\partial x_i} = 0 \quad (2)$$

$$\frac{\partial(\rho\overline{u_i})}{\partial t} + \frac{\partial}{\partial x_j}(\rho\overline{u_i}\,\overline{u_j}) = -\frac{\partial \bar{P}}{\partial x_i} + \frac{1}{\mathrm{Re}}\frac{\partial}{\partial x_j}\left((\mu+\mu_T)\left(\frac{\partial \overline{u_i}}{\partial x_j} + \frac{\partial \overline{u_j}}{\partial x_i}\right)\right) - \frac{\partial}{\partial x_j}\left(\frac{2}{3}\rho k \delta_{ij}\right) + \rho g_i \quad (3)$$

$$\frac{\partial(\rho\,\mathrm{k})}{\partial t} + \frac{\partial}{\partial x_j}(\rho\bar{u}_j\,\mathrm{k}) = \frac{1}{\mathrm{Re}}\left[(\mu + \frac{\mu_T}{\sigma_k})\frac{\partial\,\mathrm{k}}{\partial x_j}\right] - \rho\varepsilon + \underbrace{\frac{1}{\mathrm{Re}}\left(2\mu_T \bar{S}_{ij} - \frac{2}{3}\rho k\delta_{ij}\right)\frac{\partial \bar{u}_i}{\partial x_j}}_{\mathrm{II}} \quad (4)$$

$$\frac{\partial(\rho\varepsilon)}{\partial t} + \frac{\partial}{\partial x_j}(\rho\bar{u}_j\varepsilon) = \frac{1}{\mathrm{Re}}\frac{\partial}{\partial x_j}\left[(\mu + \frac{\mu_T}{\sigma_\varepsilon})\frac{\partial \varepsilon}{\partial x_j}\right] - C_{2\varepsilon}\rho\frac{\varepsilon^2}{k} + \frac{1}{\mathrm{Re}}C_{1\varepsilon}\frac{\varepsilon}{k}\underbrace{\left(2\mu_T \bar{S}_{ij} - \frac{2}{3}\rho k\delta_{ij}\right)\frac{\partial \bar{u}_i}{\partial x_j}}_{\mathrm{II}} \quad (5)$$

$$\mu_T = \mathrm{Re}\,\rho\,C_\mu\,\frac{\mathrm{k}^2}{\varepsilon} \quad (6)$$

After substituting the value of i, j indices, term (II) in the kinetic energy Eq. (4) and the dissipation Eq. (5) will be turned into the following form:

$$G = \mu_T\left[2(\frac{\partial u}{\partial x})^2 + 2(\frac{\partial v}{\partial y})^2 + 2(\frac{\partial w}{\partial z})^2 + (\frac{\partial u}{\partial y} + \frac{\partial v}{\partial x})^2 + (\frac{\partial u}{\partial z} + \frac{\partial w}{\partial x})^2 + (\frac{\partial v}{\partial z} + \frac{\partial w}{\partial y})^2\right] \quad (7)$$

3. Numerical methods

Numerical schemes such as QUICK or Power-Law which are mainly prepared for flux calculation in the orthogonal coordinate system can be equally applied in the general curvilinear coordinates. In this work, physical tangential velocity as the dependent variable is employed to solve the momentum equations. Cross derivative terms are discretized using an alternative approximation introduced by He and Salcudean [7]. An explicit method is applied for temporal terms and the pressure-velocity coupling is determined by SIMPLE algorithm.

In curvilinear coordinates, the general equation of transformation will be discretized for the dependent integer of ϕ [7].

$$\frac{\partial(\rho\phi)}{\partial t} + \nabla\cdot(\rho\vec{U}\phi) - \nabla\cdot(\Gamma\nabla\phi) + B = 0 \quad (8)$$

Considering non-orthogonal diffusion terms and sorting equations, the discretized equation will be changed into the standard form of Patankar finite volume method [6,8]. In this equation, orthogonal and non-orthogonal terms were shown with o and n, respectively [6].

$$a_p\phi_P = a_E\phi_E + a_W\phi_W + a_N\phi_N + a_S\phi_S + a_T\phi_T + a_B\phi_B + S_n + B\Delta V$$
$$a_p = a_E + a_W + a_N + a_S + a_T + a_B + a_p^0 \quad (9)$$
$$\begin{cases} a_E = a_{E,O} + a_{E,n} & a_W = a_{W,O} + a_{W,n} \\ a_N = a_{N,O} + a_{N,n} & a_S = a_{S,O} + a_{S,n} \\ a_T = a_{T,O} + a_{T,n} & a_B = a_{B,O} + a_{B,n} \end{cases}$$

In this equation, S_n contains the clauses which will remain after ordering and extracting the non-orthogonal coefficients and will be collectively located in the source term [6].

The tangent velocity $U^{\xi i}$ stands for the dependent variable of momentum equation [9].Thus the velocity vector is written as follows:

[Downloaded from ijmt.ir on 2026-11-23]

$$\vec{U} = U^{\xi_1} e_1 + U^{\xi_2} e_2 + U^{\xi_3} e_3, \qquad (10)$$

Where e_i is the unit tangential vector. The equations of momentum along with the pressure terms which are explicitly discretized will be turned into the following forms:

$$\begin{aligned}
a_P U_P^{\xi_1} &= \sum a_{nb} U_{nb}^{\xi_1} + A^{\xi_1}(P_w - P_e) + b_{U^{\xi_1}} \\
a_P U_P^{\xi_2} &= \sum a_{nb} U_{nb}^{\xi_2} + A^{\xi_2}(P_s - P_n) + b_{U^{\xi_2}} \\
a_P U_P^{\xi_3} &= \sum a_{nb} U_{nb}^{\xi_3} + A^{\xi_3}(P_b - P_t) + b_{U^{\xi_3}} \\
A^{\xi_i} &= a_{i1}\left(\frac{\partial y}{\partial \xi^j}\frac{\partial z}{\partial \xi^k} - \frac{\partial y}{\partial \xi^k}\frac{\partial z}{\partial \xi^j}\right) + a_{i2}\left(\frac{\partial z}{\partial \xi^j}\frac{\partial x}{\partial \xi^k} - \frac{\partial z}{\partial \xi^k}\frac{\partial x}{\partial \xi^j}\right) \\
&\quad + a_{i3}\left(\frac{\partial x}{\partial \xi^j}\frac{\partial y}{\partial \xi^k} - \frac{\partial x}{\partial \xi^k}\frac{\partial y}{\partial \xi^j}\right) \qquad (11) \\
&(i, j, k = 1, 2, 3 \quad \text{Clockwise})
\end{aligned}$$

In order to implement the wall function, one may assume a control volume (Figure 1), where the south surface is a solid boundary.

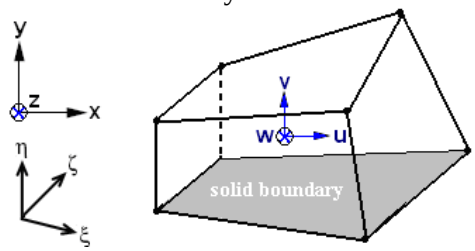

Figure 1. A view of 3D control volume

In such boundaries, in the discretized finite volume form of the momentum equations a_s is set to zero, and instead, the exerted south surface force is replaced. After some manipulation, the equation changes to the following form:

$$\begin{aligned}
a_P U_P^{\xi} &= a_E U_E'^{\xi} + a_W U_W'^{\xi} + a_N U_N'^{\xi} + a_T U_T'^{\xi} + a_B U_B'^{\xi} \qquad (12) \\
&\quad + (a_{11}\mathbf{F}_{wall}^{x} + a_{12}\mathbf{F}_{wall}^{y} + a_{13}\mathbf{F}_{wall}^{z}) + B'
\end{aligned}$$

In the above equation wall forces are calculated using the wall shear stress. It is notable that the wall shear stress is derived from the wall function. In the curvilinear coordinates wall shear stress can be obtained as below:

$$\tau_w = \begin{cases} \text{Sublayer:} & \dfrac{\mu}{\mathrm{Re}\, h_p}\left|\vec{\mathbf{U}}^{\mathbf{t}}\right| \qquad y^+ < 11.63 \\ \text{Fully Turbulence:} & \dfrac{\rho\, c_\mu^{1/4}\, \mathrm{k}^{1/2}}{\mathrm{u}^+}\left|\vec{\mathbf{U}}^{\mathbf{t}}\right| \qquad y^+ \geq 11.63 \end{cases} \qquad (13)$$

where h_p is normal distance from wall and $\left|\vec{\mathbf{U}}^{\mathbf{t}}\right|$ is tangential velocity which is estimated from Richard relation. The non-dimensional equation of y^+ is obtained from equation (14).The geometry parameters which are needed to implement the wall function such as tangent vector to the surface are according to Gant [10].

$$y^+ = \mathrm{Re}\frac{c_\mu^{1/4}\, \mathrm{k}^{1/2}\, h_p}{\nu} \qquad (14)$$

In the modeling of the free surface, Lagrangian propagation volume tracking method (VOF-PLIC) in the computational domain is used and leads to an equation of the following form [6]:

$$\begin{aligned}
&\frac{\partial C}{\partial t} + \frac{(U^{\xi_1}|S^1|\cos\alpha_1)}{Vol}\frac{\partial C}{\partial \xi_1} + \frac{(U^{\xi_2}|S^2|\cos\alpha_2)}{Vol}\frac{\partial C}{\partial \xi_2} \qquad (15) \\
&\quad + \frac{(U^{\xi_3}|S^3|\cos\alpha_3)}{Vol}\frac{\partial C}{\partial \xi_3} = 0.0
\end{aligned}$$

4. Water impact of a circular cylinder in turbulent flow

Water impact of a circular cylinder is a proper test case for studying two-dimensional two-phase free surface flow. In this work, a circular cylinder with radius of 5.5m is released to water at a constant speed of V=10 m/s. Slamming coefficient (C_S=$F/(0.5\rho V^2 D)$) obtained by Power-Law and QUICK schemes are compared with the experimental data of Campbell *et al.* [11] in Figure 2. As it is shown, QUICK is more accurate than Power-Law, especially at contact moment, i. e. h/r=0.

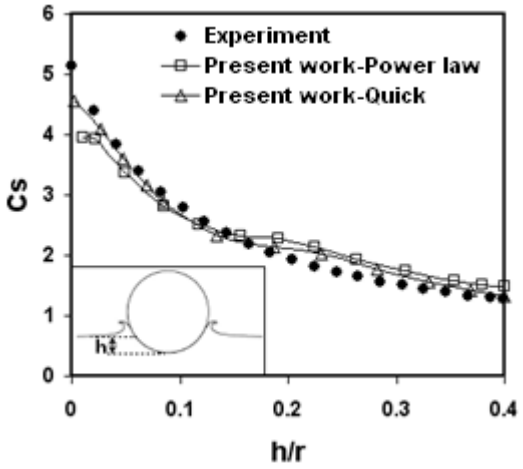

Figure 2. Comparison of slamming coefficient of the cylinder with experiment data [11], ($V = 10m/s, r = 5.5m$). *h* is the free surface height measured from the bottom of the cylinder.

Figure 3 shows the free surface shape in various non-dimensional times. The clear water spray around the cylinder shows ability of the present code and also VOF-PLIC method to anticipate this phenomenon. But, as the surface tension is not modeled, the formation and movement of the droplets are not matched well with the real shape and size.

[Downloaded from ijmt.ir on 2026-11-23]

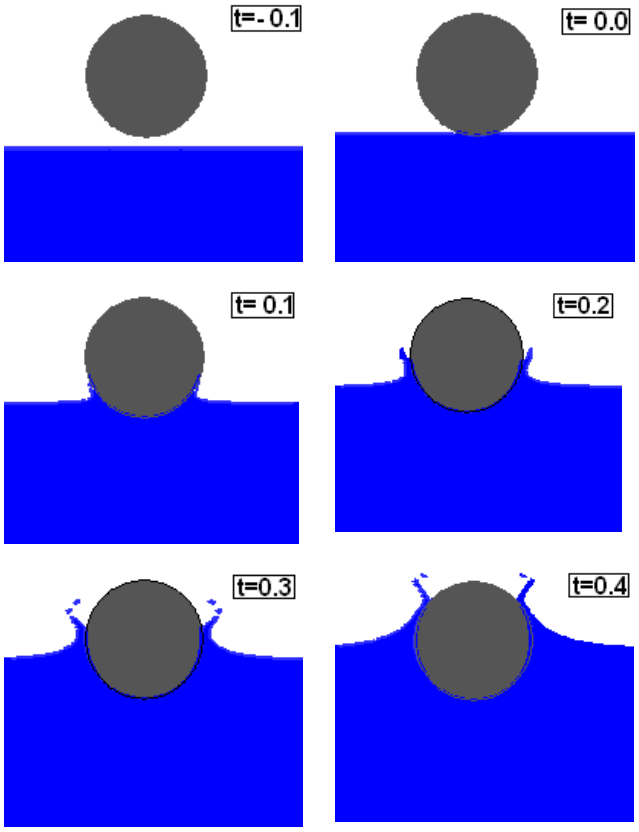

Figure 3. Free surface shape in different non-dimensional times.

5. V-shape prismatic surface

In this section, the NACA standard wedge problem is solved. The wedge geometry with deadrise angle of 20º, length of 0.9144 meters and trim angle of 2º is shown in Figure 4a, [12].

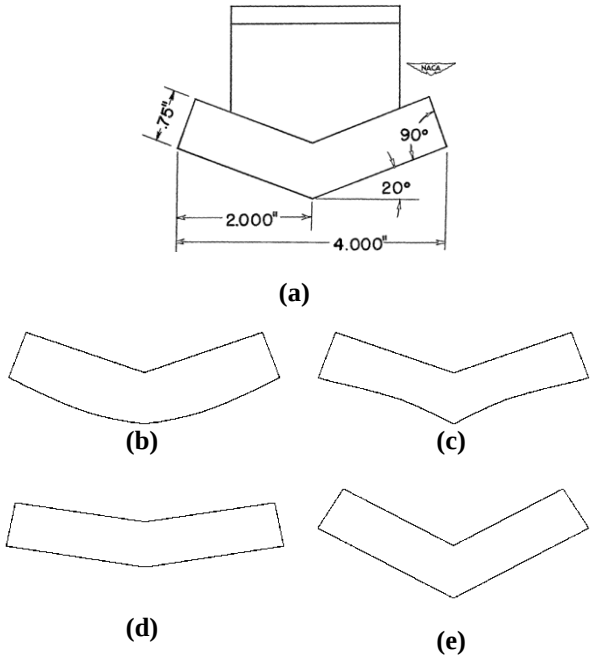

Figure 4. a) Schematic of the wedge, b) Convex curvature (Test 5), c) Concave curvature (Test 6), d) deadrise **angle 10º (Test 7), e)** deadrise **angle 30º (Test 8).**

For the first step, flow field around the given wedge is calculated with four different velocities and draft heights at the step position. Corresponding information are collected in Table 1, rows 1 to 4. Then, the average wetted lengths are compared with experimental outcomes [12] and it is seen that they are in a reasonable compatibility with experimental data, Table 2.

Table 1. Different wedge tests

Num. Test	deadrise **angle (deg)**	**Velocity (m/s)**	**Draft at step (m)**
1	20	19.86	0.01372
2	20	13.46	0.02997
3	20	16.99	0.02940
4	20	9.26	0.01132
5	convex 20	13.46	0.02997
6	concave 20	13.46	0.02997
7	10	13.46	0.02997
8	30	13.46	0.02997

Table 2. The comparison of average wetted length with experimental data.

Test	Lm	Lm (Exp),[12]
1	0.216	0.223
2	0.735	0.708
3	0.695	0.660
4	0.13	0.111

Next, the effect of the keel curvature on hydrodynamic forces was evaluated utilizing some modifications on the keel curvature and wedge angle which are depicted in Table 1, rows 5 to 8, and demonstrated in Figure 4.

The produced wave behind the wedge for tests numbers 2, 4, 5, 6, 7 and 8 is illustrated in Figure 5. The wedge in Figure 5b has the minimum velocity and draft height. As a result, it produces the shortest wave behind the wedge. The comparisons of these shapes show that when the keel curvature is concave, the produced wave does not undergo a considerable change in length and only grows in the chine of the body due to the concaveness of the surface. Also, a large hole occurs behind the wedge and a hump is produced in the front of the wedge which means that the concaveness of the keel surface propels water to edges, while the convex curve produces a longer wave behind the wedge. According to waves behind 10º and 30º wedge shown in Figs. 5e and 5f, the change of the deadrise angle has no significant effect on the wave-length. It means reduction in the deadrise angle leads to increase the width of the wave and enhancement of this angle causes the width of the wave to decrease.

[Downloaded from ijmt.ir on 2026-11-23]

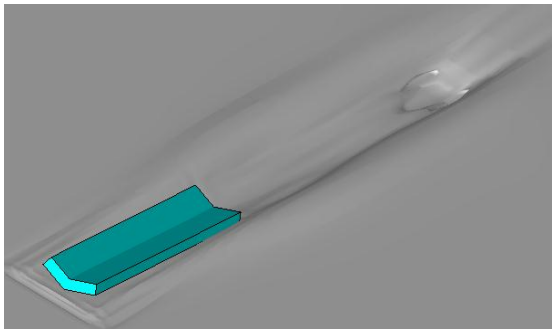

a)20° wedge (Test 2), Fr=4.3

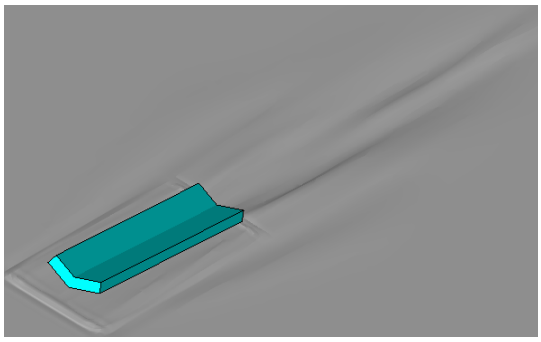

b)20° wedge (Test 4), Fr=2.96

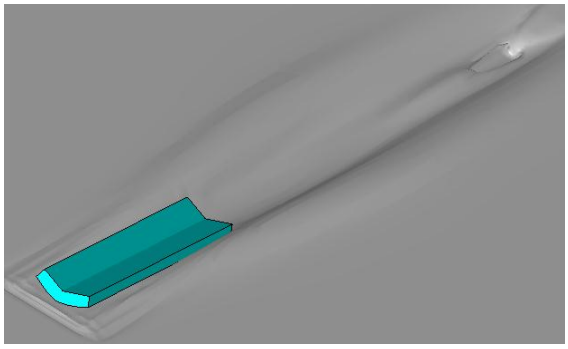

c) 20° wedge with a convex lower body (Test 5), Fr=4.3

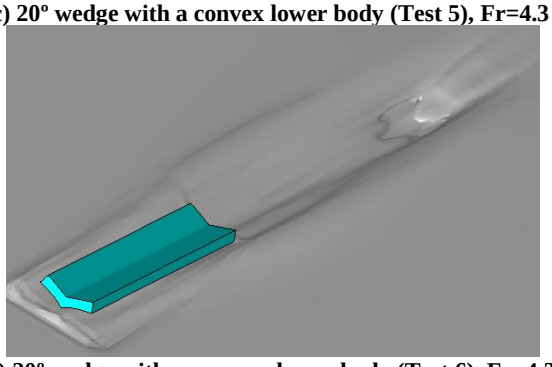

d) 20° wedge with a concave lower body (Test 6), Fr=4.3

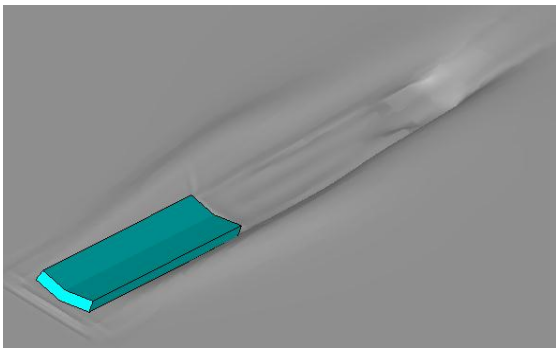

e) 10° wedge (Test 7), Fr=4.3

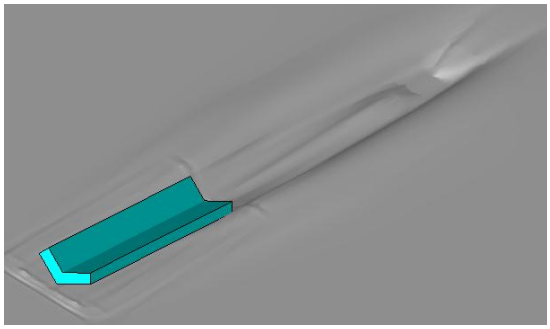

f) 30° wedge (Test 8), Fr=4.3

Figure 5. The wave produced behind wedges.

Dimensionless pressure variations (Eq. 1) at the keel line are demonstrated in Figure 6. The main difference of pressure distribution is between the cases with the deadrise angles of 10 and 30 degrees. It reveals that changing the deadrise angle has more effect on the pressure distribution than keel curvature.

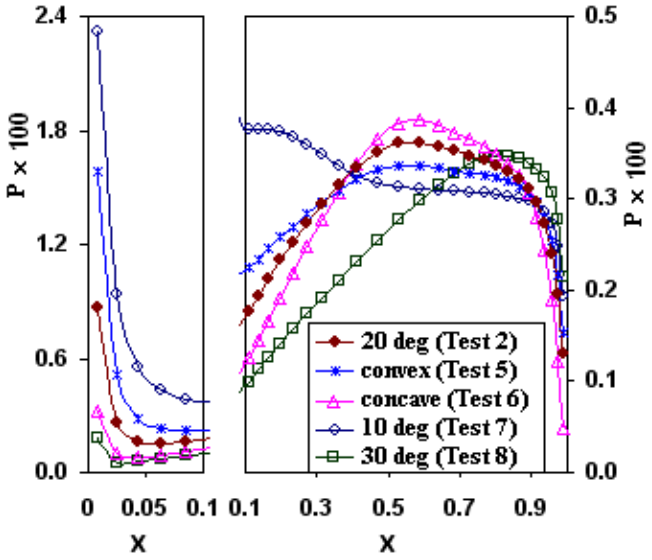

Figure 6. Pressure distribution at the keel line

The front part pressure is much higher than the other parts due to the water spray and also air and water trapping in this area. To clarify this issue the volume fraction distribution in the body is shown in Figure 7. Smaller volume fraction means more amount of air. Volume fraction of approximately 0.4 in the wedge with deadrise angle of 10 degrees and also in convex curvatures cover more area on the front of the hull which indicates more water spray. Therefore pressure at the front of this case is more than the others.

[Downloaded from ijmt.ir on 2026-11-23]

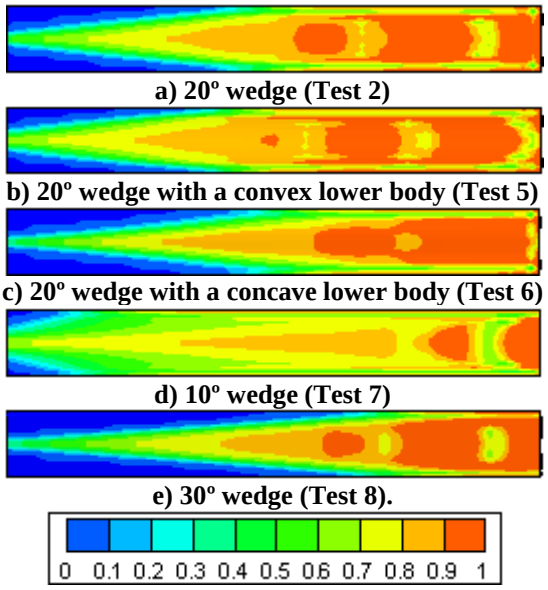

Figure 7. Volume fraction Distribution at the keel

In Table 3, the lift coefficient ($C_L=F_Z/(0.5\rho U^2 b^2)$, "$b$" stands for the body width) is compared with the experimental data [12]. Numerical errors are predictable considering the numeric state of the solution and disregarding the upper part of the wedge on which the experiments were carried out (Figure 4a).

Table 3. Numerical lift coefficient and experimental data.

Test	C_L	C_L (Exp), [12]
1	0.0149	0.0216
2	0.0381	0.0468
3	0.0347	0.0441
4	0.0159	0.0198

In order to investigate the effect of the keel curvature and different angles on lift and drag coefficient ($C_D=F_X/(0.5\rho U^2 b^2)$), the test numbers of 5, 6, 7 and 8 are carried out under the assumptions of the test number 2 whose results are presented in Table 4.

Table 4. The effect of the change of curvature on the lift and drag coefficients.

Test	C_L / C_{L2}	C_D / C_{D2}
5	1.04	2.09
6	0.95	1.12
7	1.49	0.76
8	0.66	0.41

Based on this data, drag coefficient of the convex curvature (test 5) is two times greater than simple keel profile (test 2). However, lift coefficient does not change significantly. Thus, the convex curvature is not an appropriate profile for the keel of marine vehicles.

In the test number 7 with 10º deadrise angle, maximum enhancement in the lift coefficient observed. Consequently, with reduction of the deadrise angle, the required taking-off engine power decreases. It should be noted that this curvature produces the greatest slamming force at the time of landing [13].

The numerical result of the test number 8, with 30º deadrise angle demonstrated the maximum reduction in drag coefficient in comparison with the test number 2. Moreover, it shows the greatest reduction in lift coefficient as well. It is notable that according to the numerical and experimental results of the impact problem of the wedge [14], minimum slamming force is applied to the keel at the time of landing.

6. Conclusions

Numerical results of the present work verify that the convex curvature leads to doubling the drag coefficient, whereas, the lift coefficient has not changed significantly compare with simple keel profile. Therefore, it is not an appropriate profile for the keel of planing vessels. On the other hand, decreasing the deadrise angle causes drop-off in the required engine power for take-off. It is shown that such curvature produces the greatest slamming force at the landing time. Furthermore, the largest deadrise angle produces the highest reduction in drag coefficient and the maximum diminution in lift coefficient too. Consequently, more engine power is needed for taking-off from water. Moreover, at landing time the minimum slamming force is applied to the keel. Hence, the designer should find the optimum angle and curvature of the keel to balance the hydrodynamic forces in planning and landing regimes of a surface effect vehicle.

Nomenclature

x_i	x, y and z coordinate components
U_∞	free stream velocity
L	characteristic length
Fr	froude number
Re	reynolds number
B	source term
S^i	components of control surface area
C	volume fraction function
$C_{\varepsilon 1}, C_{\varepsilon 2}, C_\mu$	turbulence model constants in k–ε model
k	turbulent kinetic energy
$\overline{P}$	mean pressure
$\overline{u_i}$	x, y and z components of mean velocities, i=1,2,3
$\vec{\mathbf{U}}^{\mathbf{t}}$	tangential velocity

Greek symbols

ρ	fluid density
ε	turbulent kinetic energy dissipation rate

[Downloaded from ijmt.ir on 2026-11-23]

σ_k turbulent Prandtl number of k

σ_ε turbulent Prandtl number of ε

τ_w wall shear stress

μ molecular dynamic viscosity

μ_T turbulent viscosity

Subscripts

l values in the liquid phase

i, j is 1, 2, 3 or x, y, z directions

7. References

1- Gao, H., Gu, H., Guo, L., (2003), *Numerical study of stratified oil–water two-phase turbulent flow in a horizontal tube*, Int. J. Heat and Mass Transfer. Vol.46(4), p. 749-754.

2- Jones, W. P., Launder, B.E., (1972), *The prediction of laminarization with a two-equation model of turbulence*, Int. J. Heat and Mass Transfer. Vol.15(2), p 301–314.

3-Yuk, D., Yim, S.C., Liu, P.L.F., (2006), *Numerical modeling of submarine mass-movement generated waves using RANS model*, Computers & Geosciences. Vol.32(7), p. 927-935.

4- Ciortan, C., Wanderley, J., Soares, C.G., *(*2007), *Turbulent free-surface flow around a Wigley hull using the slightly compressible flow formulation,* Ocean Engineering. Vol.34(10), p. 1383-1392.

5- Rhee, S. Makarov, H. B., Krishinan, P. H., Ivanov, V., (2005), *Assessment of the volume of fluid method for free-surface wave flow*, J. Marine Science and Technology, Vol.10(4), p. 173-180.

6- Nikseresht, A. H., Alishahi, M. M., Emdad, H., (2008), *Complete flow field computation around an ACV (Air Cushion Vehicle) using 3D VOF with Lagrangian propagation in computational domain*, J. Computer & Structure. Vol.86(8), p. 627-641.

7- He, P., Salcudean, M., (1994), *A numerical method for 3D viscous incompressible flows using non-orthogonal grids*, Int. J. For Numerical Methods in Fluids. Vol.18(5), p. 449-469.

8- Nikseresht, A. H., Alishahi, M. M., Emdad, H., (2009), *Generalized curvilinear coordinate interface tracking in the computational domains*, *J. Scientica Iranica*. Vol.16(1), p. 64-74.

9- Rodi, W., Majimdar, S., Schonung, B., (1989), *Finite volume method for two dimensional incompressible flow with complex boundaries*, Computer Methods Applied in Mechechanic and Engineering. Vol.75(1), p. 369-392.

10- Gant, S., (2002), *Development and application of a new wall function for complex turbulent flows*, PhD thesis; University of Manchester, Institute of Science and Technology, Manchester, UK.

11- Campbell, I. M. C., Weynberg, P. A., (1980), *Measurement of parameters affecting slamming*, Rep. No. 440, Wolfson Unit for Marine Technology, Southampton, UK..

12- Chambliss, D. B., Boyd, G. M., (1953), *The planing characteristic of two V-shape prismatic surface having angles of deadrise of 20 and 40 degree*, Langley Aeronautical Laboratory; NACA TN 2876, Washington.

13- Moradi, H., Nikseresht, A. H., (2006), *Investigation of the dead-rise angle effects on the slamming force of flying boat symmetric landing*, J. Mechanics and Aerospace. Vol.3(3), p. 61-72. (In Persian).

[Downloaded from ijmt.ir on 2026-11-23]